Degradation mechanisms of $LiNi_{0.5}Mn_{0.3}Co_{0.2}O_2$/graphite battery in real-life driving scenarios

Guo, Jia; Xu, Yaolin; Liu, Yanchen; Li, Pengwei; Che, Yunhong; Li, Yaqi; Pedersen, Kjeld; Schuck, Götz; Kristensen, Peter Kjær; Baran, Volodymyr; Sun, Yanan; Adelhelm, Philipp; Stroe, Daniel Ioan

Published in:
Energy Storage Materials

DOI (link to publication from Publisher):
10.1016/j.ensm.2025.104441

Publication date:
2025

Document Version
Publisher's PDF, also known as Version of record

Energy Storage Materials 80 (2025) 104441

Contents lists available at ScienceDirect

Energy Storage Materials

journal homepage: www.elsevier.com/locate/ensm

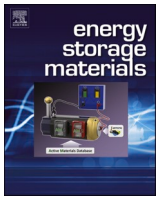

Degradation mechanisms of $LiNi_{0.5}Mn_{0.3}Co_{0.2}O_2$/graphite battery in *real-life* driving scenarios

Jia Guo [a,b,c,*], Yaolin Xu [b,g,*], Yanchen Liu [b], Pengwei Li [d], Yunhong Che [a,e], Yaqi Li [a,c], Kjeld Pedersen [c], Götz Schuck [f], Peter Kjær Kristensen [c], Volodymyr Baran [i], Yanan Sun [b,h], Philipp Adelhelm [b,h], Daniel-Ioan Stroe [a]

[a] Department of Energy, Aalborg University, 9220 Aalborg, Denmark
[b] Department of Chemistry, Humboldt University of Berlin, 12489 Berlin, Germany
[c] Department of Materials and Production, Aalborg University, 9220 Aalborg, Denmark
[d] Department of Chemistry and Bioscience, Aalborg University, Aalborg, 9220 Denmark
[e] Department of Chemical Engineering, Massachusetts Institute of Technology, Cambridge, MA, 02139 USA
[f] Department Structure and Dynamics of Energy Materials, Helmholtz-Zentrum Berlin für Materialien und Energie GmbH, Hahn-Meitner-Platz 1, 14109 Berlin, Germany
[g] Department of Applied Physics, Aalto University, Espoo, 00076 Finland
[h] Joint Research Group Operando Battery Analyses (CE-GOBA), Helmholtz-Zentrum Berlin für Materialien und Energie (HZB), 14109 Berlin, Germany
[i] Deutsches Elektronen-Synchrotron (DESY), Notkestrasse 85, Hamburg, Germany

ARTICLE INFO

Keywords:
NMC 532/graphite
Degradation mechanisms
Real-life driving
WLTC profile
Depth of Discharge (DOD)

ABSTRACT

Understanding the aging mechanisms of lithium-ion batteries (LIBs) in *real-life* driving scenarios is the key to advancing battery design and management for electric vehicles. This work studies in detail the aging modes of commercial LIBs under *real-life* driving scenarios with a standardized World Harmonized Light Vehicle Test Cycle (WLTC) discharging procedure. Combined results from electrochemical analyses, post-mortem, and *operando* characterization show that a large depth of DOD (100 %) leads to significant structural changes, especially Ni-O bond length and coordination number, of NMC532 cathode materials and hence rapid degradation related to active material loss, while a low DOD level (45 %) results in intensified interfacial degradation, both leading to a limited battery cycle life (<900 and <1600 equivalent full cycles (EFCs), respectively, under 45 % and 100 % DoDs). In contrast, a medium DOD (75 %) results in balanced electrode and interface degradations and significantly enhanced cycling stability (>2200 EFCs under 75 % DoDs). Besides, we also emphasized that in *real-life* driving, the loss of active materials primarily originates from the cathode. These findings reveal that balancing the electrode and interfacial degradations are crucial for extending battery lifetime in practical applications. This work provides mechanistic insights into the degradation of LIBs under *real-life* operating conditions, guiding the rational design and optimization of cycling protocols in battery management systems (BMSs) for advanced battery development.

1. Introduction

The success of lithium-ion batteries (LIBs) has promoted the booming electrification of various sectors, encompassing portable electronic devices [1], electric vehicles (EVs) [2,3], and grid energy storage [4]. Currently, the most widely used LIB chemistry currently consists of a $LiNi_{0.5}Mn_{0.3}Co_{0.2}O_2$ (NMC532) cathode paired with a graphite anode [5]. The large market share is mainly attributed to its mature manufacturing process and high energy density [6]. Even under some operating conditions, NMC532 batteries can deliver improved Coulombic efficiency, reduced capacity degradation, and higher energy density compared to LFP batteries [7]. In *real-life* driving scenarios, however, the different usage scenarios combined with complex degradation processes makes the prediction of performance and safety properties difficult, especially considering the long service life of batteries [8,9]. Moreover, the battery aging modes under *real-life* driving conditions differ from those observed in laboratory tests. Recent study show that compared to constant-current discharge with same average current, battery discharging under *real-life* can extend battery lifetime by 37 % [10]. This poses challenges to engineering study based on traditional

* Corresponding authors.
E-mail addresses: jia.guo1@imperial.ac.uk (J. Guo), yaolin.xu@aalto.fi (Y. Xu).

https://doi.org/10.1016/j.ensm.2025.104441
Received 1 May 2025; Received in revised form 1 June 2025; Accepted 30 June 2025
Available online 1 July 2025

laboratory data, especially battery electrochemical modeling. Hence, it becomes imperative to comprehensively understand the aging mechanisms for widely used commercial batteries under *real-life* driving conditions. This is crucial for designing an advanced battery management system (BMS) that simultaneously enhances durability and safety in electric vehicles.

In the laboratory, constant current and constant voltage (CC-CV) charging, along with a high constant current (CC) (> 0.5C) discharging, are commonly used protocols for battery aging, which makes the graphite anode more likely to crack [11,12]. As a result, most electrochemical models for battery degradation are based on graphite crack [13,14]. However, in real-world driving conditions, battery aging modes may be different. EV batteries stress differently under *real-life* driving conditions, making it essential to account for various practical factors involved in a vehicle's driving process, e.g., loadings and driving ranges, when investigating the battery aging mechanisms. The World Harmonized Light Vehicle Test Cycle (WLTC) comprehensively considers a vehicle's driving conditions (i.e., peak, off-peak, and weekend), road types (i.e., urban, rural, and motorway), and a wide range of vehicle categories and driving habits (N) [15,16]. The process involves converting speed vs. time curves to current vs. time curves, simulating battery discharge under Class 3 vehicle conditions. The current profiles of batteries under WLTC discharge, replicating *real-life* EV driving scenarios, are shown in Fig. S2.

In *real-life* driving, factors like the distance between home and work (i.e., the driving range) influence the user's driving habits. The typical practice is to fully charge the battery while the EV is parked and then gradually discharge it during driving to different depths of discharge (DODs), depending on the driving distance. Hence, it becomes imperative to consider the influence of DOD on battery degradation. At present, the effect of DOD on battery lifetime remains unclear. Several studies have reported conflicting findings regarding the impact of DOD on battery degradation. Some studies suggest that a smaller DOD range accelerates battery aging due to notable volume changes and increased interfacial impedance [17–20], while others observe the opposite result, where battery aging intensifies with an enlarged DOD range [21–23]. The lack of clarity in test results poses a significant obstacle to designing an effective battery management system (BMS) for lifetime extension. The influence of driving range on battery lifetime is not solely determined by battery electrode materials but also by the operation conditions. It is essential to elucidate the detailed influence of DOD on the battery aging modes in *real-life* driving.

In this study, we utilized WLTC procedures that replicate *real-life* driving conditions to discharge commercial cylindrical NMC532/graphite LIBs. By examining the influence of DODs, e.g., 100 %, 75 %, and 45 % DOD, on battery aging, our findings deviate from the existing literature, revealing slower aging under moderate DODs and accelerated aging with both large and small DODs. Through comprehensive electrochemical analyses, including capacity evaluation, electrochemical impedance spectroscopy (EIS), and charging-discharging curve analysis, we elucidated the impact of DOD on battery aging modes and identified the primary aging mechanisms under different DODs. Our proposed aging modes and mechanisms were validated through post-mortem analyses, and *operando* characterization such as *operando* X-ray diffraction (XRD) and *operando* synchrotron X-ray absorption spectroscopy (XAS) that revealed DOD's impact on the crystal structure and local coordination of electrode materials. This holistic approach contributes to a mechanistic understanding of NMC532/graphite battery aging under *real-world* driving conditions, offering guidance for future battery and BMS design.

2. Results and discussion

2.1. Aging of NMC532/graphite LIBs

To investigate the influence of DODs on battery performance in *real-life* driving scenarios, we utilized distinct sets of WLTC procedures to discharge the batteries at 45 °C, which included 11, 8 and 4 instances of WLTC to reach 100 %, 75 %, and 45 % DOD, respectively, as illustrated in Fig. 1a-c. The voltage curves during cycling for different DOD levels are depicted in Fig. 1d. Despite the gradually increasing voltage ranges along with battery aging, a larger DOD leads to an extended discharge voltage range. Furthermore, the battery state of health (SOH) is evaluated after each 100 equivalent full cycles (EFCs), as illustrated in Fig. 1e. Specifically, the battery with a medium DOD (75 %) maintains an 85 % SOH even after 2200 EFCs, whereas the battery SOH drops to 80 % after 900 and 1600 EFCs, respectively, when discharged to a low (45 %) and a high (100 %) DOD. Meanwhile, the battery with a small DOD of 45 % operates at a narrower and higher voltage range of 3.68–4.2 V during cycling. In comparison, the voltage range extends to 3.53–4.2 V at 75 % DOD and further to 2.75–4.2 V at 100 % DOD (Fig. 1f). Although the battery surface temperature fluctuations under these three conditions are all within 2 °C, it is evident that as the DOD decreases, the amplitude of temperature fluctuation increases, and the overall battery temperature also rises (Fig. S3). We also replicated the experiment at 35 °C and obtained a similar result that 75 % DOD leads to much better cycling stability than that with 45 % and 100 % DODs, as shown in Fig. S4. This finding contradicts empirical knowledge established in battery testing experiences that batteries typically undergo an accelerated capacity decay with an increasing DOD [24–26]. This can be related to the low average discharge current of 0.17 C under a WLTC procedure and hence extended cycling period under *real-life* driving conditions. The detailed degradation mechanisms under WLTC discharge to different DODs are studied in the following.

Battery charging and discharging curves, along with incremental capacity-differential voltage (IC-DV) curves, are used to identify the battery aging modes. As depicted in Fig. S5a–c, the battery discharging plateau exhibits a noticeable shortening and descending trend during the aging process, corresponding to the loss of active materials and the increase in battery polarization [27], respectively. Moreover, the shortening of the voltage plateau is evident in the reduction of the peak intensity of the IC curve (Fig. S5d-f), which represents the loss of active materials. The drop in the voltage plateau aligns with the rightward shift of the IC curve peak and the upward shift of the DV curve (Fig. S5g–i), which indicates the battery polarization. This is particularly noticeable in the 100 % DOD and 45 % DOD cases in comparison to the 75 % DOD, signifying a faster occurrence of polarization and active material loss. The polarization and loss of active materials can be further studied using EIS on the cell level. *Operando* EIS was performed for the battery cells after every 100 EFCs. Fig. 2a–c show the evolution of the Nyquist plots at a 70 % state of charge (SOC) of the batteries operating with different DODs. The measured EIS spectra are fitted with an equivalent circuit model (Fig. 2d), and the evolution of the interface impedance R_{sei} (Fig. 2e) and charge transfer impedance R_{ct} (Fig. 2f) are obtained. The detailed fitting results are presented in Figs. S6–S8. It is clear that a larger DOD accelerates the increase of R_{ct}, while a smaller DOD accelerates an increase in R_{sei}. Besides, the *operando* EIS results were also measured at 10 %, 30 %, 50 %, and 90 % SOC to map the impedance variation along with varying SOCs and DODs during WLTC aging, which is shown in Fig. 2g-l. A large DOD range, specifically 100 % DOD, accelerates the increase in charge transfer impedance at almost all SOCs. This behavior is attributed to changes in the structure of active materials [28]. A small DOD, e.g., 45 % DOD, accelerates the increase in the interface impedance, which can be attributed to the electrode surface film formation. Furthermore, machine learning is used to quantify the correlation between battery SOH and the parameters R_{sei} and R_{ct} under different DODs. The results, as shown in Fig. S9, indicate that under 100 % DOD aging, there is a distinct relationship between the decrease in SOH and the increase in R_{ct}. In comparison, under 45 % DOD aging conditions, a strong correlation is observed between the decrease in SOH and the increase in R_{sei}. This further proves that battery aging at 45 % DOD is most closely related to increased interface impedance. At 100 %

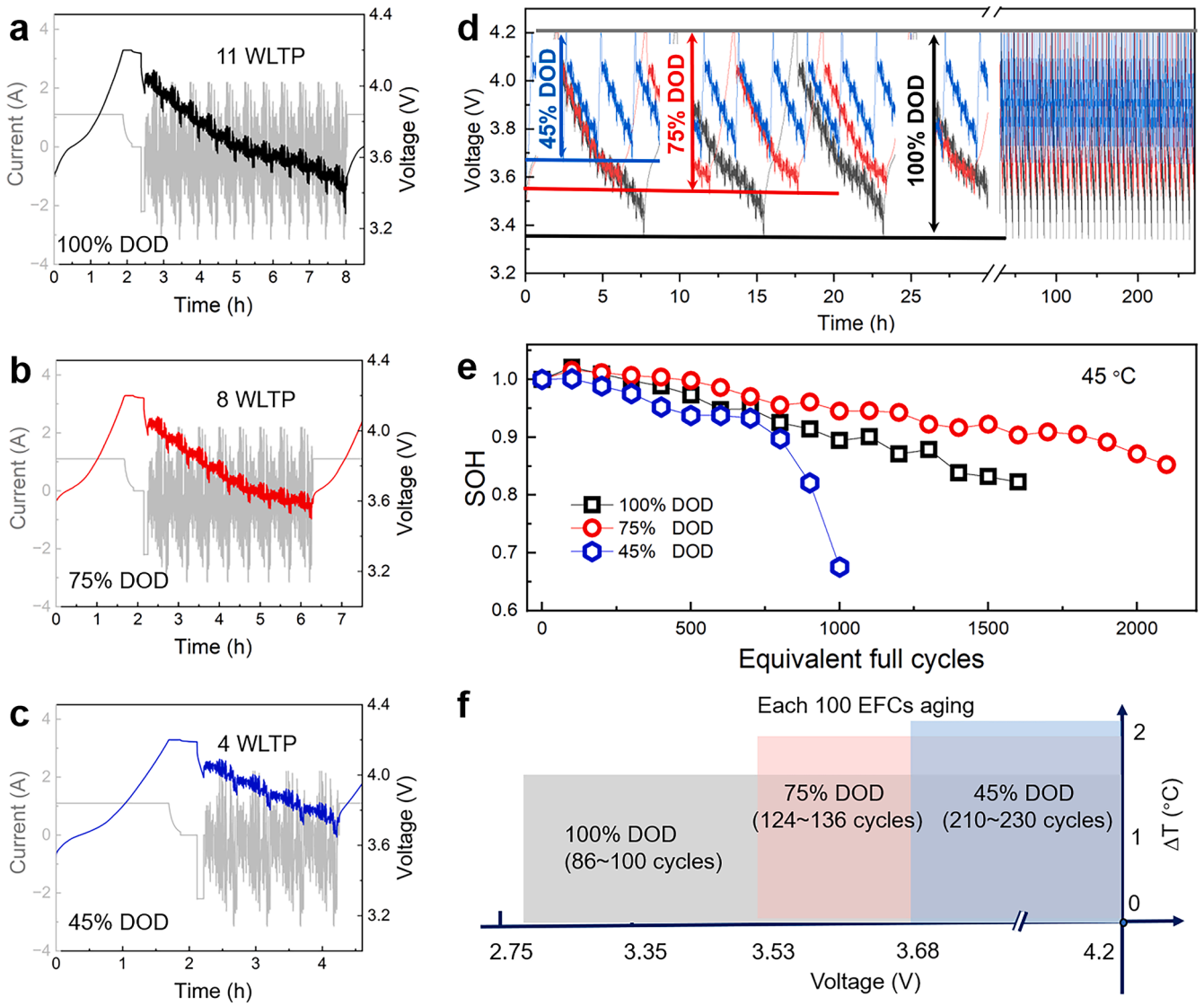

Fig. 1. Battery aging protocols and health evolution in *real-life* driving scenarios. Battery current and voltage curves during aging under WLTC discharge to (a) 100 %, (b) 75 %, and (c) 45 % DOD; (d) Battery voltage curves with different DODs; (e) SOHs of batteries aged at different DODs; (f) Operating voltage ranges and battery surface temperature fluctuations under different DODs.

DOD, battery aging is strongly correlated with slow charge transfer processes. Furthermore, at 35 °C, the impedance of the battery exhibits a similar phenomenon (Fig. S10).

At 45 °C, the performance at 100 % DOD clearly exceeds that at 45 % DOD, while at 35 °C, the performance at 100 % DOD is comparable to or even inferior to that at 45 % DOD. This indicates that at 45 °C, a lower DOD results in a higher battery temperature, approaching the critical temperature of electrolyte instability and thereby exacerbating interfacial degradation.

In short, under WLTC discharge with a larger DOD range, the battery aging process is primarily affected by the loss of active materials, while battery aging with a smaller DOD range is dominated by the instability of electrode-electrolyte interfaces.

2.2. Aging of electrode-electrolyte interfaces

We performed a post-mortem analysis of aged batteries to investigate the detailed changes of battery materials and interfaces to unravel the battery aging mechanisms. To facilitate reliable comparison and identification of the main aging modes under different operating conditions, four batteries aged to the same SOH, i.e., 90 %, subjected to two aging temperatures 35 °C and 45 °C and three DOD ranges i.e., 100 %, 75 %, and 45 % were investigated. These batteries are denoted as T35–45 % DOD, T35–100 % DOD, T45–75 % DOD, and T45–100 % DOD, respectively, as outlined in Table 1. Here, four batteries were used at two different temperatures, rather than three batteries at the same temperature, based on statistical considerations. This approach minimizes experimental errors and the influence of uncertainties as much as possible, and it has also been used in previous publications [29,30]. The cycling performance for batteries aged at 35 °C and 45 °C, respectively are shown in Fig. S8, which exhibits a consistent aging trend with the long-term aging tests discussed above (see Fig. 1e and Fig. S4).

It is interesting to note that cycling at a small DOD (45 %) worsens the cycling stability and battery lifetime, as shown in Fig. S11, which is also consistent with the battery aging tests (Fig. 1e). This is attributed to the higher operating voltage range increase under a smaller DOD (Fig. 1f). The SEI is typically formed and accumulated during charging within the voltage range of 3.8V to 4.2V [31]. Therefore, cycling at a small DOD also undergoes intensified SEI film-forming processes.

The thicknesses of the CEI and SEI films on the NMC532 and graphite electrodes, respectively, were revealed with TEM (Fig. 3a), and the general morphology of the battery positive and negative electrode

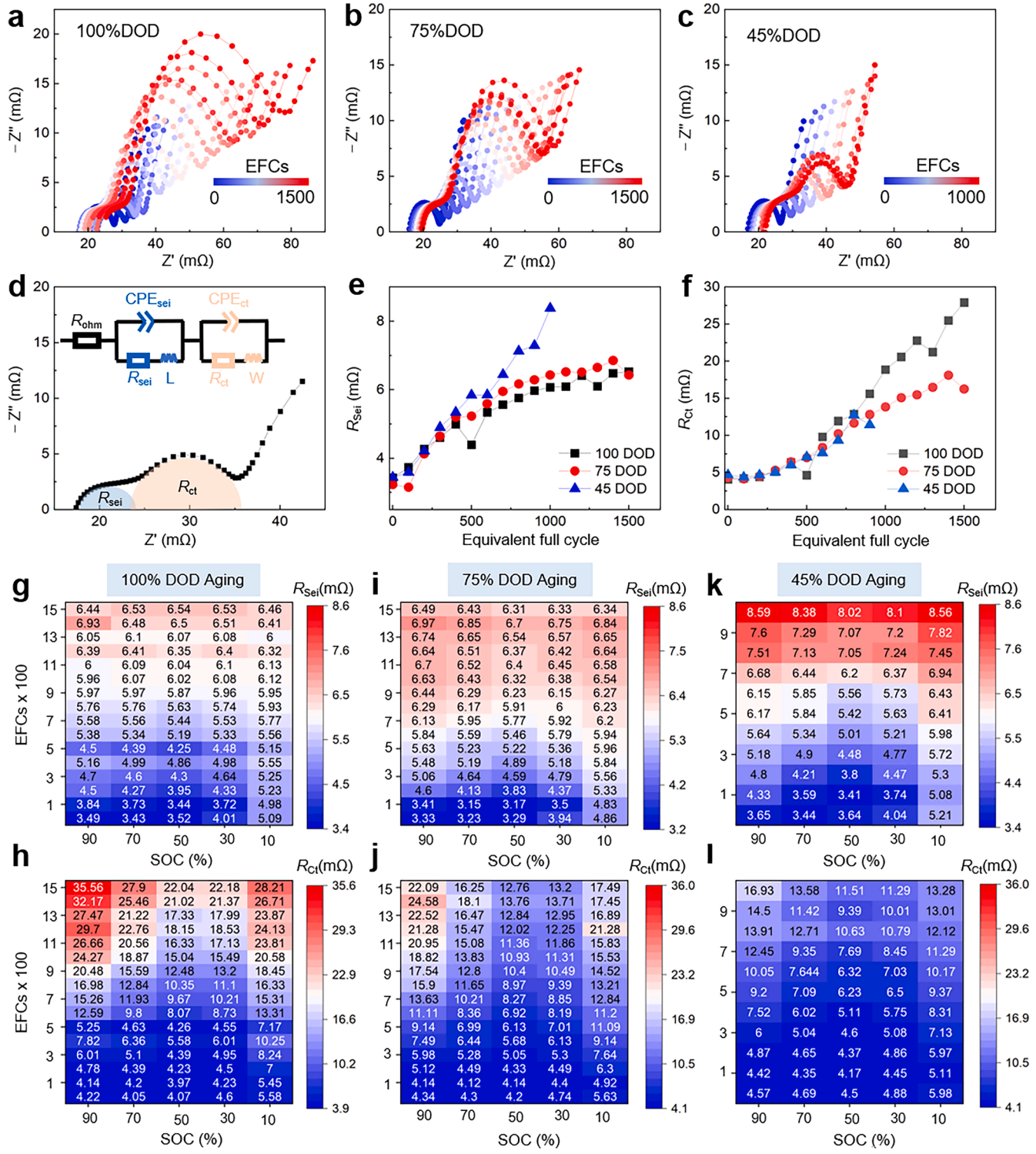

Fig. 2. The Nyquist plots at 70 % SOC of batteries aged during cycling at 45 °C. (a) 100 %, (b) 75 %, and (c) 45 % DOD during WLTC aging. (d) The equivalent circuit mode used to fit the Nyquist plots, and the fitted results of (e) R_{sei} and (f) R_{ct}. The operando EIS results at 90 %, 70 %, 50 %, 30 %, and 10 % SOC of, batteries aged at 100 % (g, h), 75 % (i, j), and 45 % (k, l) DOD, respectively.

Table 1
The batteries used for post-mortem analysis.

Temperature	45 % DOD	75 % DOD	100 % DOD
35 °C	T35–45 % DOD		T35–100 % DOD
45 °C		T45–75 % DOD	T45–100 % DOD

particles are shown in Fig. S12. The CEI film thickness ranges from 3 to 10 nm. In comparison, the SEI film is much thicker, up to ~100 nm. Specifically, the batteries aged at T35–45 % DOD and T45–75 % DOD have thicker CEI films, 8.3 nm and 5.7 nm, respectively, which are thicker than 3.5 nm and 4.7 nm observed, respectively, at T35–100 % DOD and T45–100 % DOD. The SEI film after aging with T35–45 % DOD and T45–75 % DOD are 105.5 nm and 78.3 nm, respectively, which is

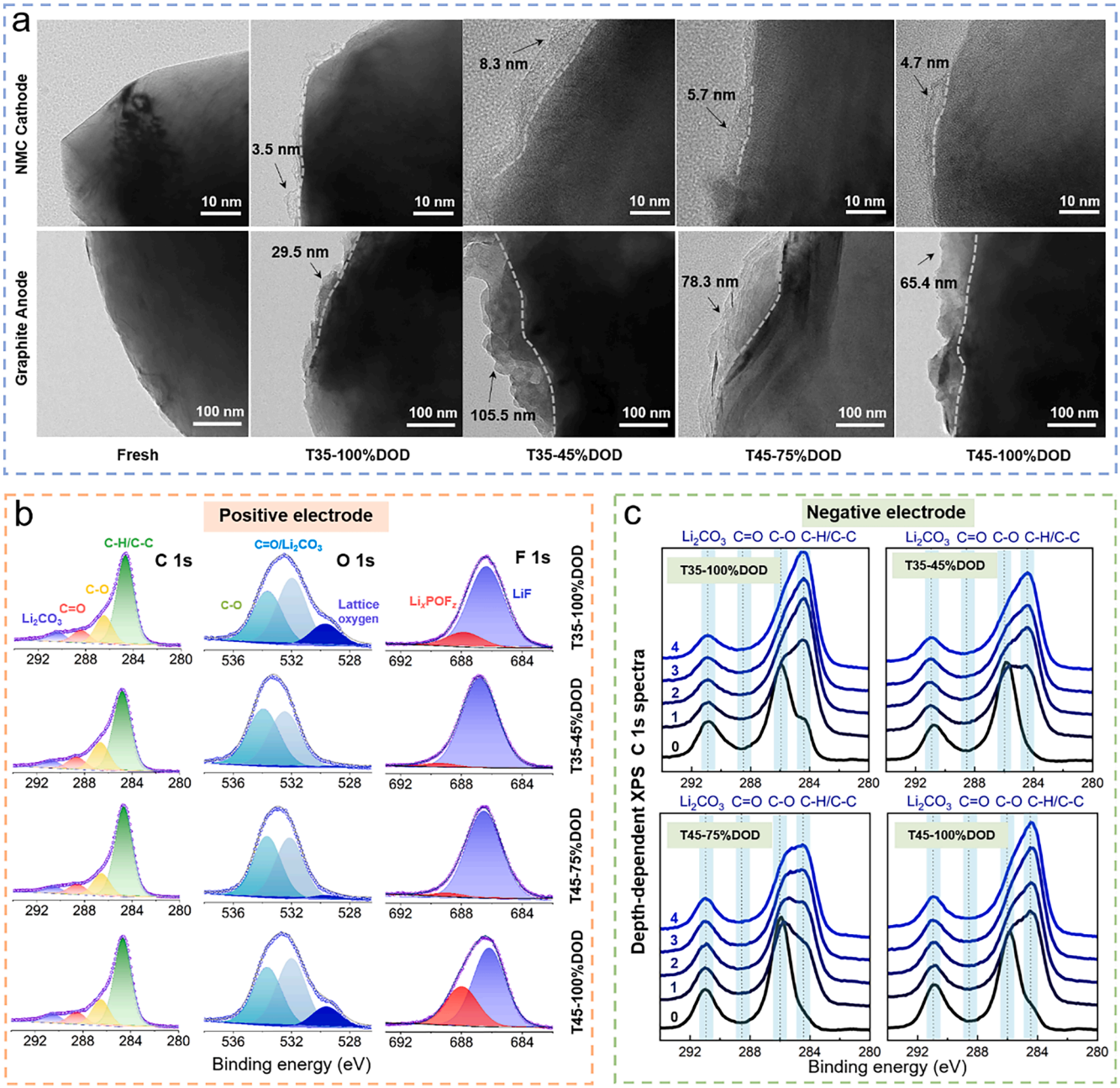

Fig. 3. TEM and XPS investigations of the interfacial layers on the aged electrodes under various conditions: T35–100 % DOD, T35–45 % DOD, T45–75 % DOD, and T45–100 % DOD. (a) TEM images of aged NMC cathodes and graphite anodes; (b) XPS results for the positive electrodes; (c) Depth-dependent XPS C 1s spectra of the negative electrodes.

considerably thicker than the 29.5 nm and 65.4 nm observed at T35–100 % DOD and T45–100 % DOD, respectively.

XPS was employed to unveil the composition of the interfacial film on the electrodes. Typically, the interfacial films (SEI and CEI) exist at the electrode surface, consisting of both inorganic Li salts and organic compounds, such as LiF (~ 686.8 eV in F 1s), Li_2CO_3 (~ 291.1 eV in C 1s, and), C=O (~ 288.3 eV in C 1s, and 532.9 eV in O 1s), C–O (~ 285.8 eV in C 1s, and ~ 534.7 eV in O 1s), and Li_xPOF_z (~ 688.6 eV in F 1s) [32]. As shown in Fig. 3b, the CEI layer of the aged cathode has a similar composition. A noticeable distinction is the content of lattice oxygen (i.e., peak centered at 529.5 eV) in the O 1s spectrum, which originates from the NMC532 cathode materials, is significantly higher for the T35–100 % DOD and T45–100 % DOD aged electrodes compared to that under T35–45 % DOD and T45–75 % DOD aging. This indicates a thinner CEI film formed on the surface of the NMC532 cathode aged with a lower DOD, which is consistent with the TEM results.

To investigate in detail the chemistry and structure of the SEI film on graphite anode, XPS depth profile analysis was carried out and the results are depicted in Fig. S13-S14. The C 1s XPS depth profile results are shown in Fig. 3c. Before etching, the primary component in the C 1s spectra is C–O. After the initial etching, the peak corresponding to the C–H/C–C bond in the C 1s spectrum becomes more pronounced, particularly under the aging conditions of T35–100 % DOD and T45–100 % DOD. This is attributed to the enhanced contribution from the graphite particles underneath the SEI layer. In contrast, the C 1s spectra, characterized by the C–H and C–C bond peaks remain unchanged after two etching sessions for the graphite anodes aged at T35–45 % DOD and T45–75 % DOD. This observation also suggests the presence of a thicker

SEI film for batteries aged at T35–45 % DOD and T45–75 % DOD, consistent with the analysis above.

2.3. Aging of electrodes and active materials

When the battery SOH drops to 90 %, the morphology of the aged graphite negative electrode does not exhibit apparent degradation (particle cracking and electrode thickening) (Fig. S15) compared with the fresh electrode, which could be attributed to the low average discharge current of 0.17 C along with its high SOH. This is different from our previous research findings [13,33], where laboratory aging experiments typically use a constant current of 1C or even higher, making the cracking of the graphite anode the primary cause of battery degradation. In contrast, material degradation is evident for the aged positive electrodes (Fig. 4). At a larger DOD (100 %), the positive electrodes show more severe secondary particle rupture, as shown in Fig. S16-S19, and the statistical results are summarized in Fig. 4a. At 35 °C, the cathode particles aged at 100 % DOD were nearly entirely fractured, whereas after cycling with 45 % DOD, the cathode particles remained partially intact. This might be correlated with the number of battery EFCs, with 45 % DOD undergoing fewer EFCs (900 EFCs) than 100 % DOD (1300 EFCs) to reach 90 % SOH. A similar phenomenon occurs at 45 °C. A deep DOD (100 %) accelerates the cracking and pulverization of NMC532 secondary particles. As a result, the positive electrode becomes significantly thicker than the fresh electrode, as shown in Fig. 4b-c. In particular, the electrode thickness increases by 26 % under T45–100 % DOD aging. Meanwhile, the fragmentation of secondary particles and the thickening of the electrode will increase the charge transfer resistance during electrochemical operation, which is in line with the impedance analysis in Fig. 2. These morphological changes of the aged NMC532 cathodes are associated with the mechanical stress exerted on the secondary particles during battery charging and discharging, typically induced by the change of crystal structure and phase transformation of the NMC532 materials [34].

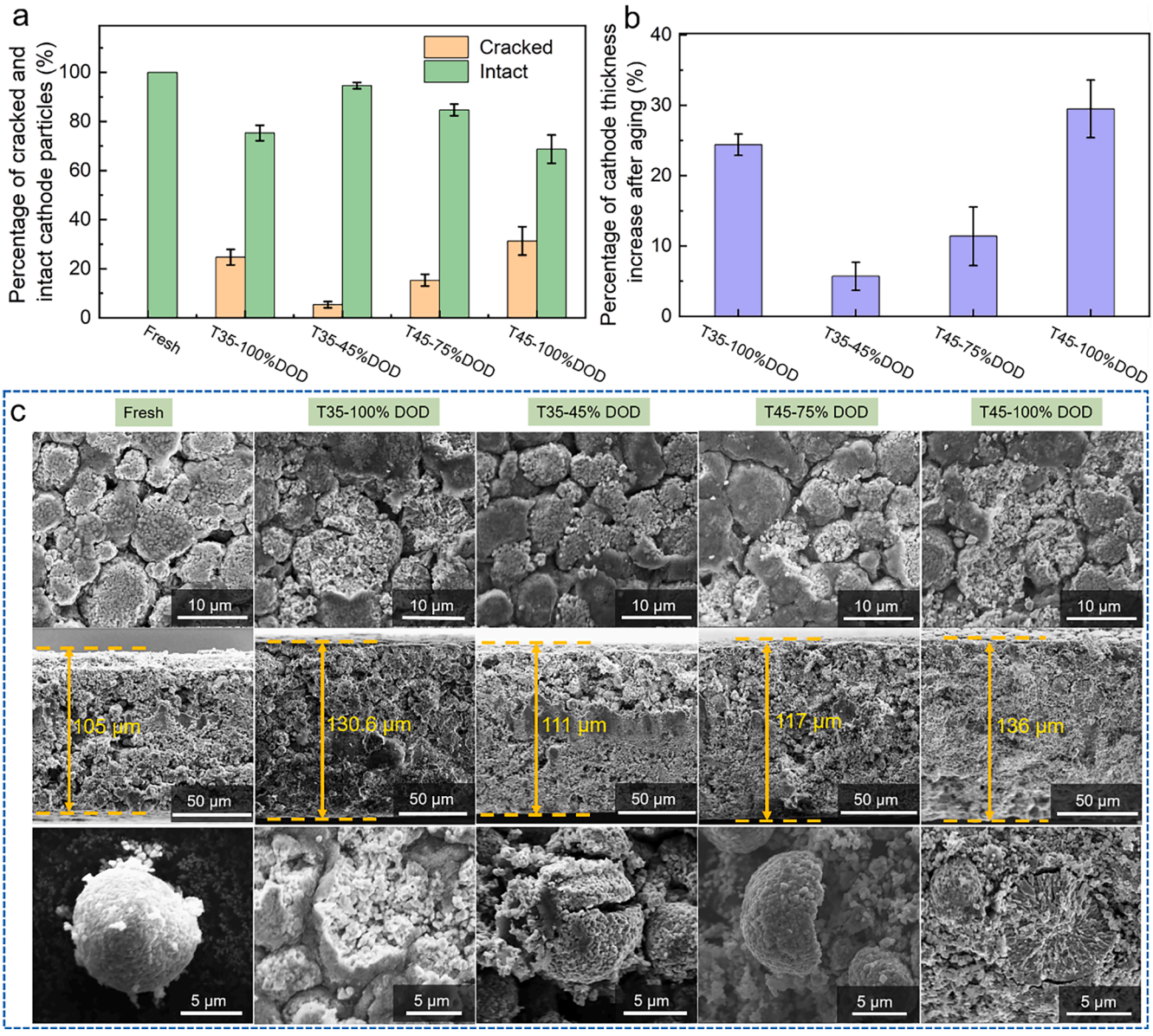

Fig. 4. Morphology of NMC532 positive electrodes and materials. (a) Statistical results on the percentage of cracked NMC532 particles based on the SEM images in Fig. S16-S19; (b) Quantified results on the percentage of cathode thickness increase after aging; (c) SEM images of the electrode surface (top), electrode cross-section (middle), and particle morphology (bottom) of fresh and aged NMC532 cathode under different conditions: T35–100 % DOD, T35–45 % DOD, T45–75 % DOD, and T45–100 % DOD.

Ex situ synchrotron XRD and XAS were carried out to investigate the crystal structure changes of the aged graphite and NMC532 electrodes. The results are demonstrated in Fig. 5, which shows minimal alteration in the XRD patterns of the aged graphite anodes and no apparent changes can be observed in the dominant (002) peak, indicating the preservation of graphitic structure and layer spacing [35]. Additionally, the full width at the maximum (FWHM) of the (002) peak remains fairly stable, suggesting limited fragmentation of the graphite crystalline areas [36,37]. Unlike the typical battery aging tests with constant current protocols, where high currents tend to exacerbate graphite anode cracking and exfoliation [38], battery aging related to graphite anode degradation is somewhat limited under *real-life* driving conditions.

Ex situ synchrotron XRD patterns of the NMC532 cathodes (Fig. 5b) show an apparent shift of the (003) peak toward smaller 2θ and hence larger *d*-spacing after aging, and the shift is more significant as the DOD increases. This observation suggests that during cycling with a larger DOD, there is a notable increasing trend of the *c*-value of NMC532. This is caused by the formation of the rock salt phase, leading to the loss of active materials and charge transfer impedance increase, which is consistent with the EIS results presented in Fig. 2. *Ex situ* XAS provides additional information on the local crystal structure changes, especially the alterations of dominant elements, during the phase transition. The Ni, Co, and Mn K-edge EXAFS results are shown in Fig. 5c–e, while the corresponding energy states are shown in Fig. S20. As the DOD increases, there is a noticeable reduction in the Ni–O radial distance of the aged NMC532 positive electrodes. These results suggest that the battery aging involves an increase of *d*-spacing and a reduction of the Ni–O distance. In contrast, the Co and Mn K-edge EXAFS results exhibit minimal changes. This indicates that the primary source of active material loss in the battery arises from the phase change, attributed to alterations in the Ni element within the crystal structure, of the NMC532 cathode material.

In short, the graphite anode material maintains structural stability throughout the aging process under real-life driving conditions. In contrast, the aging of NMC532 cathode material is evident with an increase in the lattice spacing and reduction of Ni–O distance, which is aggravated at an elevated DOD, resulting in the loss of active cathode materials.

To delve deeper into the impact of DOD on the crystal structure change of NMC532 materials during battery charge and discharge, we performed *in-situ* XRD and *in-situ* XAS for the positive electrode. The *in-situ* XRD patterns are displayed in Fig. 6a. The (003) peak shifts to the right during charging and to the left during discharging. This phenomenon is attributed to the extraction of Li^+ from NMC532, reducing the layer distance during charging, and the reverse process happens during battery discharging. The DOD influences the content of Li-ion insertion and extraction, and hence the unit cell volume of the NMC532 crystal structure and the layer spacing. Under larger DODs, the NMC crystal structure undergoes more significant changes.

As discussed above, the active material loss during battery aging is related to the state change of transition metal elements, especially Ni. Herein, *ex-situ* XAS is employed to investigate the energy and bond length variations of transition metal elements of NMC cathode at various SOCs during battery charge and discharge with various DODs, and the results are shown in Fig. S21. All transition metal elements (Ni, Mn and Co) exhibit fluctuated energy states during battery dis/charging, and the energy states are elevated when the battery SOC level is high. Among these, Ni exhibits the most significant energy fluctuation. This is aligned with findings in the literature [39], where Ni contributes the most to the energy state. The *ex-situ* EXAFS results are shown in Fig. S22. There exists an oxygen competition mechanism between Ni and Mn, with Ni atoms exhibiting the highest coordination with O when the battery is fully charged, while Mn atoms have the lowest coordination number with O. Also, it appears that Co does not demonstrate notable energy variations or alterations in Co–O bond length throughout the charge and discharge cycles. Moreover, in the charged state, the bond lengths of

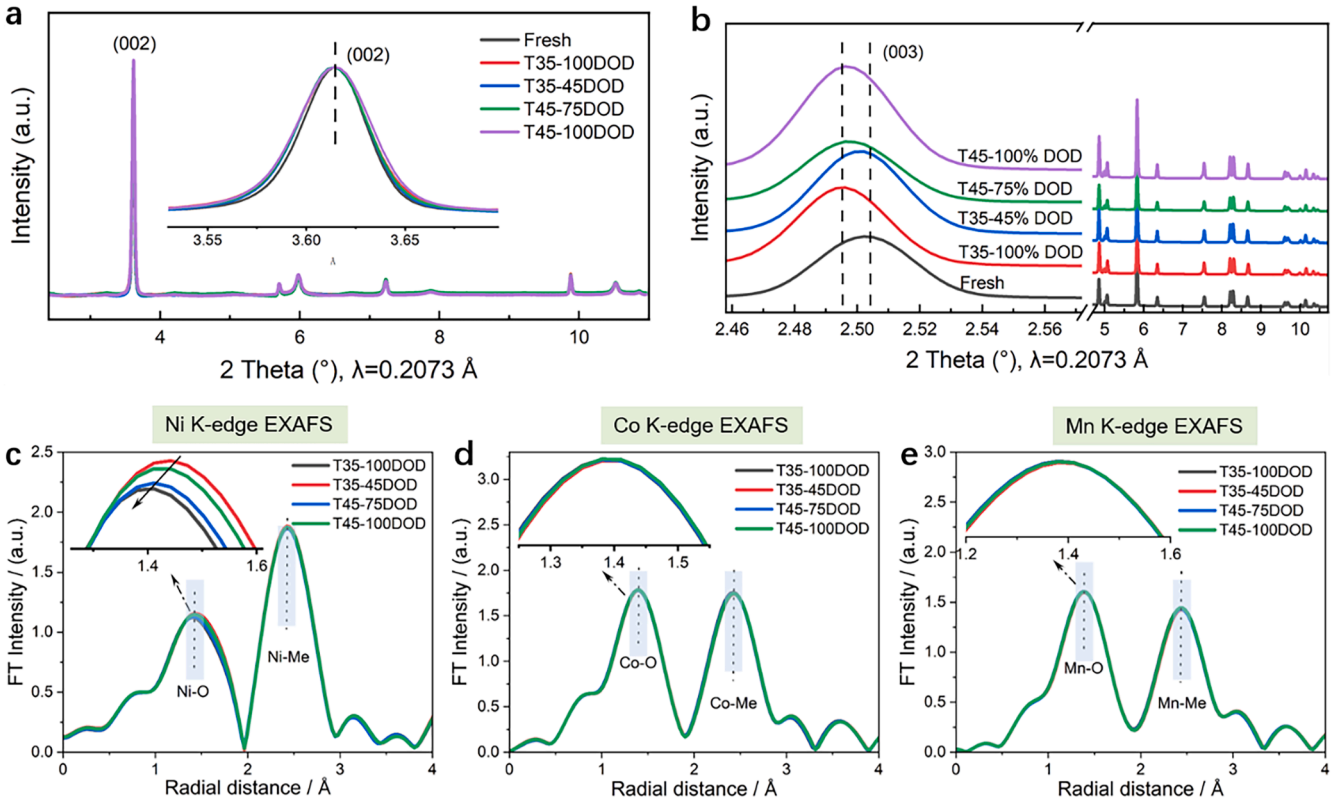

Fig. 5. *Ex situ* synchrotron XRD patterns of (a) aged graphite negative electrodes and (b) aged NMC532 positive electrodes; *ex situ* (c) Ni, (d) Co, and (e) Mn K-edge EXAFS results of NMC532 cathodes.

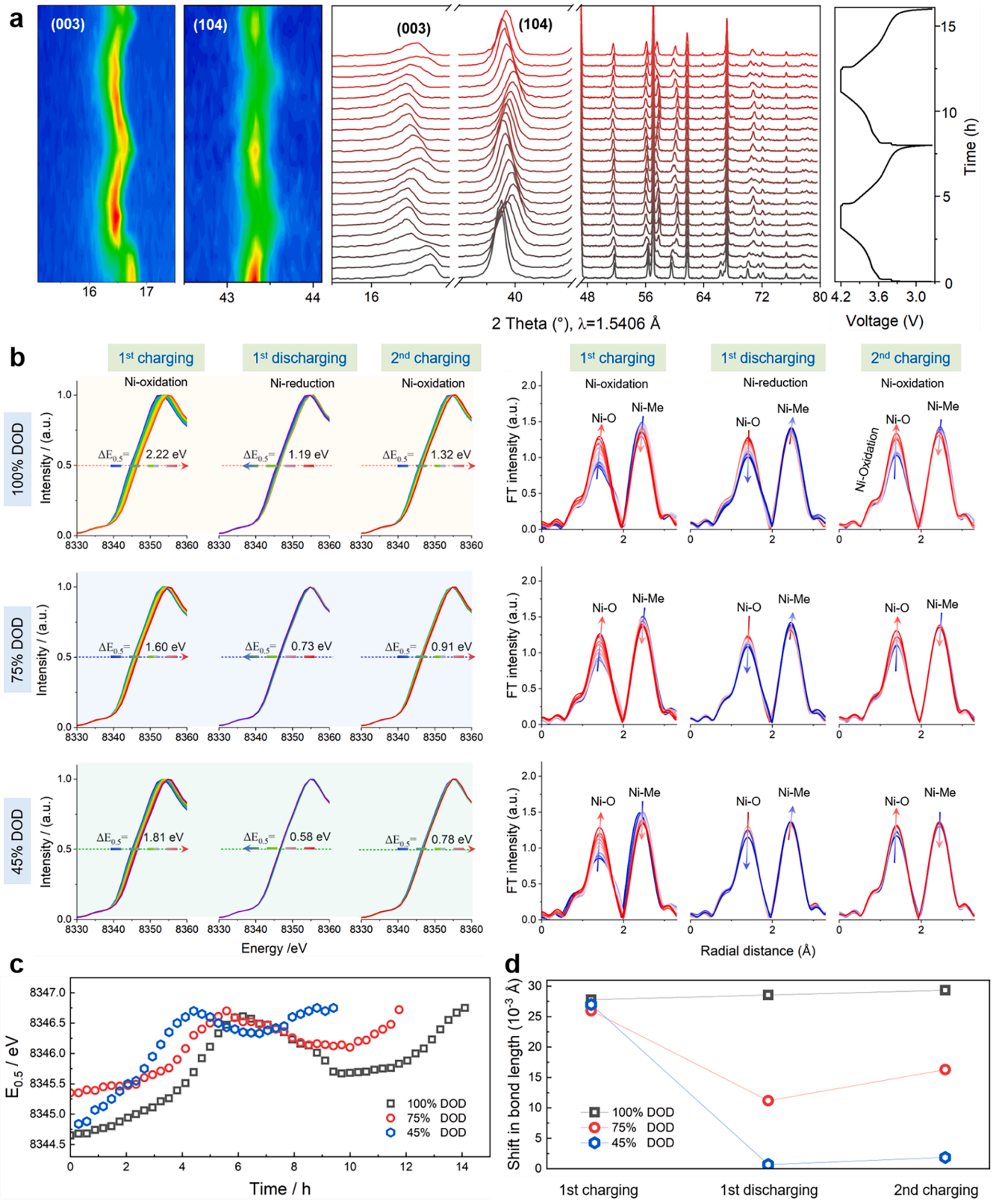

Fig. 6. *Operando* XRD and XAS analyses of the NMC532 cathode during two charge-discharge cycles. (a) XRD patterns and contour plots of NMC532 cathode at the selected 2θ ranges, highlighting the evolution of (003) and (104) peaks, during charge and discharge; (b) Ni K-edge XAS spectra and EXFAS analysis (During charging, Ni oxidizes occurs in the arrow's direction, during discharging, Ni reduction in the direction with the arrow.); Evolution of (c) the Ni K-edge half-peak intensity ($E_{0.5}$) and (d) the shift in Ni–O bond length.

Ni–O and Mn–O bonds are shorter than that in the discharged state. This is related to the change in NMC layer spacing. Therefore, the change in Ni–O bond length and energy state is the primary source of stress in the NMC532 crystal structure during battery operation.

Herein, *in-situ* Ni K-edge XAS spectra and EXAFS results of the NMC electrodes under 100 % DOD, 75 % DOD, and 45 % DOD are shown in Fig. 6b. In general, the Ni K-edge XAS spectra transit to a higher energy state during discharging and to a lower one during discharging. Note that, during the initial charging, the energy state changes are different between the batteries, which are associated with the differences in their rest periods before testing. Therefore, the subsequent discharge-charge cycle is used for quantitative analysis of the energy state fluctuations during battery cycling. The Ni K-edge energy state change at half-peak intensity ($E_{0.5}$) is employed to quantify the energy state change of the Ni element, which reaches 1.19 eV, 0.73 eV, and 0.58 eV for 100 % DOD, 75 % DOD, and 45 % DOD, respectively, during discharging, and 1.32 eV, 0.91 eV, and 0.78 eV, respectively, for 100 % DOD, 75 % DOD, and 45 % DOD during charging. Such energy state variations manifest a linear relationship between the energy state change and the DOD, which can be correlated with the extent of Li-ion insertion and extraction in the NMC532 cathode materials.

The $E_{0.5}$ variations of Ni K-edge along battery cycling with different DODs are illustrated in Fig. 6c. The difference in energy changes during the first charging process may be attributed to the resting period between cell activation and testing, during which some lithium ions may re-intercalate into the graphite anode. In the subsequent discharge and charge processes, it can be observed that as the DoD increases, the energy state changes of Ni atoms in the cathode material become more pronounced. This is because higher DoD involves the extraction of more lithium ions, requiring Ni to undergo greater redox activity, resulting in more significant changes in valence state and local electronic structure. This exacerbates the instability of the Ni element during the battery aging process. The energy state of Ni atoms is associated with the bond length and coordination number with the surrounding O and other transition metal (Mn and Co) elements. Upon the initial battery charging, the Ni–O bonds undergo a gradual increase, while the Ni–Me (Ni–Mn and Ni–Co) bonds gradually shorten. In addition, the O coordination number of Ni increases along the delithiation of the cathode. During the subsequent discharge process, the reverse process is observed, i.e., the length of the Ni–O bond shortens, and the oxygen coordination number of Ni is reduced. As the DOD decreases from 100 % to 45 %, both the change in bond length and the coordination number decrease in the following charging and discharging processes, and the quantitative results are shown in Fig. 6d. This indicates that a higher degree of lithiation and delithiation in the cathode material results in more pronounced variations in the Ni–O bond length. At the same time, the energy level transitions of Ni atoms become increasingly significant during this process, which increases the instability of the chemical environment of Ni atoms.

The DOD influences the unit cell parameters, particularly the *c*-value and layer-spacing of the NMC532 crystal structure. These changes, coupled with the degree of Li^+ deintercalation, contribute to variations in the Ni atom energy state and O coordination number, as well as the Ni–O and Ni–Me bond lengths. With an increase in the DOD, these changes become more pronounced, amplifying the instability of the state of atomic Ni. Therefore, a large DOD accelerates the crystal structure deformation of NMC532 cathode material. This observation differs from previous experience. Typically, high-nickel cathodes undergo severe structural degradation at high voltages [40]. However, for NMC532, due to its lower nickel content, the structural degradation appears to be more closely associated with structural changes during the cycling process.

2.4. Discussions on the degradation modes vs DoDs under WLTC discharge

This study reveals the aging mechanisms of batteries for EV applications under WLTC discharge to simulate real-life driving conditions, including short-, medium-, and long-distance driving, at the levels of the full cell, electrodes, and materials. As summarized in Fig. 7, cycling at a smaller DOD of 45 %, the battery operates at a higher average SOC level and within a higher voltage range, resulting in side-reactions and accelerating battery aging. The specific manifestation is the thickening of both the SEI and CEI films, which leads to an increased interfacial impedance. At a larger DOD (100 %), the battery operates at a lower average SOC, the average voltage and temperature are low, leading to limited parasitic interfacial reactions and thinner SEI/CEI films. However, due to the large DOD experienced and the resulting significant stress during the process, the cathode material particles undergo severe pulverization. These stresses occur because Ni–O bonds undergo more significant changes in energy state and bond length with a larger DOD, deteriorating the crystal structure stability and accelerating loss of active material.

This work contributes to battery and BMS design advancements toward performance improvements in real-life applications.

(i). This study unveils the aging modes and detailed materials and interfacial degradation mechanisms of NMC/graphite LIBs under dynamic conditions simulating *real-life* driving, guiding the rational design of battery materials and interfaces to suppress the corresponding degradation process and thus to enhance the battery operational stability in EV applications.

(ii). A moderate DOD balances battery degradation related to loss of active materials and continuous electrode-electrolyte interface degradation, which can significantly extend and even double the battery lifetime in *real-life* driving conditions. It will stimulate further optimization of DOD and, more broadly, BMS design toward battery lifetime enhancement.

Of course, this work has limitations that deserve future research endeavors. For instance, the optimal DOD for maximizing the battery lifetime is still to be investigated and identified; the WLTC discharge current profile simulates but deviates from *real-life* driving, and the extracted current profiles from field data are required to guide battery testing and BMS optimization in real-world applications.

3. Conclusion

This study, simulating the operational conditions of EV batteries in real-life driving scenarios, offers a detailed investigation into the degradation of commercial LIBs under varying temperatures and depths of discharge. Key findings from the study stress the significant influence of driving habits, particularly DOD, on EV battery lifetime. Unlike the results from traditional laboratory tests, under real-driving conditions, the graphite anode structure remains relatively stable, whereas the NMC532 cathode undergoes significant structural changes, leading to a loss of active material, particularly at large DODs. A smaller DOD extends battery operation at a high voltage range, accelerating battery aging rooted in the electrode-electrolyte interface degradation. *In situ* test analysis unveils the predominant role of Ni element in influencing the phase transformation of the NMC532 cathode under large DOD conditions. Specifically, a larger DOD results in increased energy floating and bond-length changes, elevating the instability of the Ni element in the NMC532 crystal structure.

In short, the work provides new mechanistic insights into battery aging under *real-life* driving conditions and prompts optimization of battery testing protocols. It contributes to the advancement of battery and BMS design toward enhancing the efficiency and lifetime of batteries in practical applications.

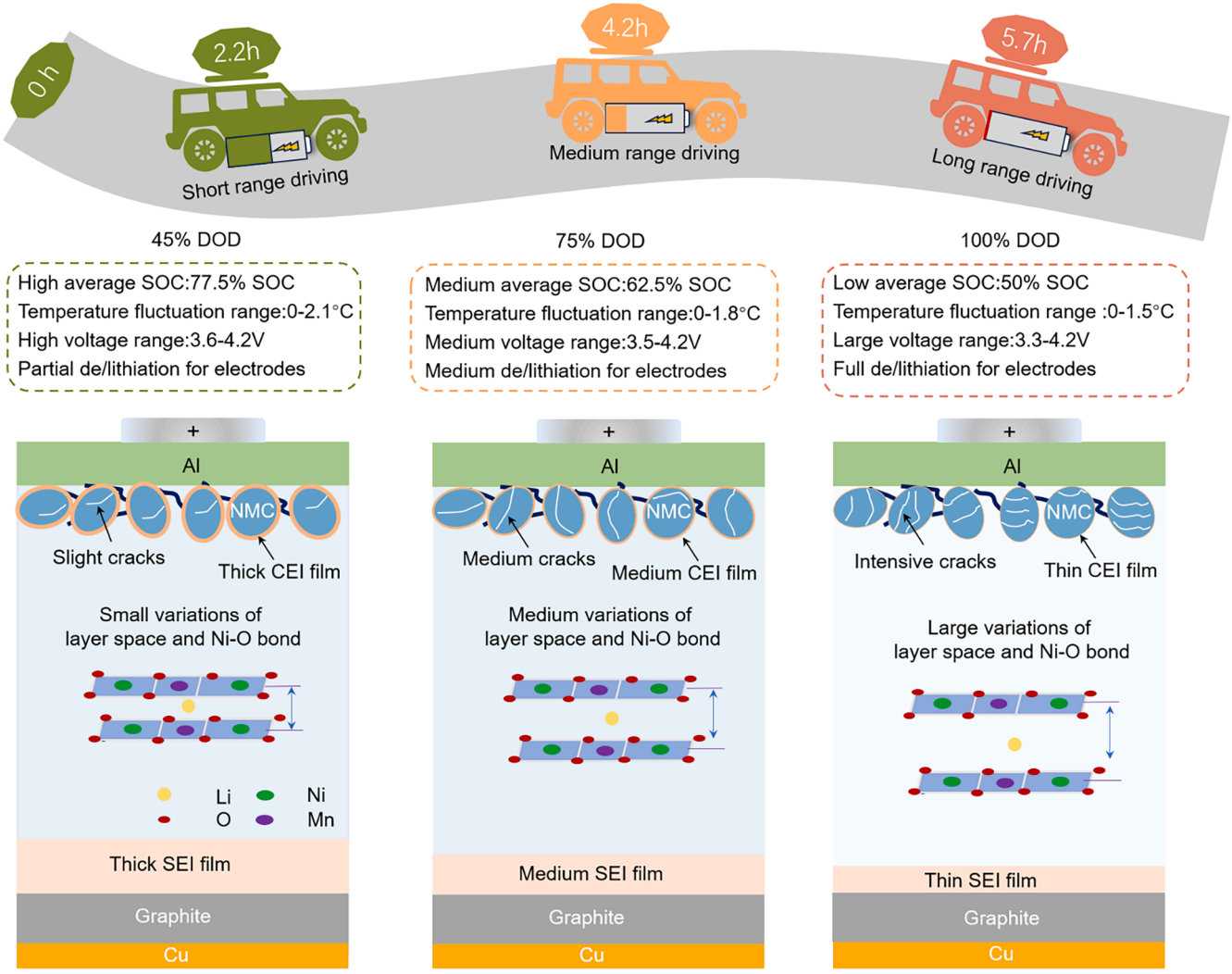

Fig. 7. The battery degradation mechanisms under different driving scenarios: short-range driving, medium-range driving, and long-range driving.

4. Experiment Section

4.1. Full battery tests

Aging test. Commercial batteries (HDCNR18650-2200-3.7V-3C) were employed for battery aging tests. The cathode material is Li($Ni_{0.5}Mn_{0.3}Co_{0.2}$)O_2 (NMC532) and the anode is graphite. The batteries were charged with 0.5 C constant current to 4.2 V, and then were charged at constant voltage until the current was reduced to 0.05 C. This is the standard charging protocol provided in the battery datasheet, which also serves as the basis for the battery management system. We define the battery's capacity after standard protocol charging as 100 % SOC. The batteries were discharged with a dynamic WLTC current profile. The DODs were set at about 100 % (11 WLTC), 75 % (8 WLTC), and 45 % (4 WLTC) at 35 °C and 45 °C respectively, as shown in Fig. S2. The details are included in our previous publication [35]. The temperature selection was based on the typical battery temperature range of 30–45 °C during real-world driving [41].

Reference performance test (RPT). Before cycling and after every 100 equivalent full cycles (EFCs), RPTs were conducted to evaluate the battery's state of health (SOH) in a 25 °C climate chamber. The RPT included a capacity test and an EIS test. For the capacity test, batteries were charged with a constant current-constant voltage (CC-CV) protocol until the current dropped to <0.11 A during the 4.2 V CV stage. Following an hour of relaxation, the batteries were subjected to CC discharging to 2.75 V, followed by an additional hour of relaxation. Charging and discharging were performed once at rates of 0.25 C, 0.5 C, and 1 C, respectively. Subsequently, the EIS test was carried out after every capacity test. The batteries were fully charged to 100 % SOC using a CC-CV charging protocol at a current of 1 C. They were then discharged to 90 %, 70 %, 50 %, 30 %, and 10 % SOC before EIS tests were conducted at these SOCs using a Digatron potentiostat. The frequency range for EIS was set between 6.5 kHz and 10 mHz. The EIS data were fitted using ZSimpWin software, with fitting errors all below 5 %.

4.2. Post-mortem analyses

Four additional cells were aged and disassembled after aging to 90 % SOH for post-mortem analysis [35]. The four batteries were aged at 35 °C and 45 °C, respectively. At 35 °C, the batteries were aged at 45 % DOD and 100 % DOD. At 45 °C, the batteries were aged at 75 % DOD and 100 % DOD. The post-mortem analysis process involved several steps. Initially, the batteries were discharged to 2.75 V using a constant current of 0.1 C. Subsequently, the batteries were transferred to a glove box within an argon atmosphere. In the next step, the batteries were disassembled, and the graphite anode and NMC532 cathode were taken out and washed separately using diethyl carbonate (DEC). Lastly, the washed electrodes were dried for 24 hours and sealed in bags in the glove box, preparing them for subsequent physio-chemical characterization.

Depth-Dependent XPS Analysis: The XPS depth profile of aged graphite electrodes was performed using Ar-ion beam etching to access subsurface information. A Specs XR50 system equipped with a non-monochromated Al Kα X-ray source (hv = 1487 eV) and a Phobos 1501D-DLD electron detector were utilized for the analysis. Peak fitting of the XPS spectra was conducted using CasaXPS software, applying a Shirley-type background correction. Charging-induced peak shifts were adjusted based on the C–C bond at 284.91 eV in the C 1s spectrum. Quantification of chemical species was carried out using relative sensitivity factors (R.S.F.) to correct peak areas representing substance concentrations. The R.S.F. values for C 1s, O 1s, F 1s, and Li 1s were 1, 2.93, 4.43, and 0.0568, respectively.

***Ex situ* X-ray powder diffraction (XRD).** *Ex*-situ XRD measurements were conducted at the Powder Diffraction and Total Scattering Beamline P02.1, PETRA III (DESY, Hamburg) [42]. For the measurements, graphite powder and NMC powder recovered from cycled electrodes were filled into glass capillaries with a diameter of 0.8 mm. Data collection was performed using the Varex XRD 4343CT (150 × 150 μm^2 pixel size, 2880 × 2880 pixel area, CsI scintillator directly deposited on amorphous Si photodiodes). LaB6 SRM 660c standard from NIST was used for calibration of the measurement configuration. Calibration and integration of the 2D data were performed using the DAWN software [43].

***Ex situ* X-ray Absorption Spectroscopy (XAS).** *Ex*-situ Ni, Co, and Mn K-edge XAS were carried out at room temperature at KMC-2 at BESSY II, Germany, employing both transmission and fluorescence modes. Reference spectra for energy calibration were obtained before and after each sample measurement. Using Athena software, XAS spectra were derived by subtracting the pre-edge background from the overall absorption and normalizing to the spline fit. The k^2-weighted extended X-ray absorption fine structure (EXAFS) was Fourier-transformed over the limited range of k from 3 to 11 $Å^{-1}$. The data processing was performed using Athena software [44]. The k^2-weighted EXAFS was Fourier-transformed over the limited range of k from 3 to 8 $Å^{-1}$.

Scanning Electron Microscope (SEM). Electrode morphologies were examined using a Zeiss EVO 60 field emission SEM at an accelerating voltage of 15 kV. Cross-sectional samples were prepared by precisely slicing the electrodes with a sharp blade to ensure clean cuts for imaging.

Transmission Electron Microscopy (TEM). Imaging of the graphite and NMC electrodes was conducted using a Philips CM200 and a FEI Talos F200S.

4.3. Operando Characterization

***Operando* X-Ray Diffraction (XRD).** XRD patterns were acquired utilizing a STOE Stadi MP diffractometer featuring a Ge (111) double-crystal monochromator (Mo Kα radiation, λ = 0.70930 Å). Transmission geometry was employed for measurements of the pristine NMC532 sample, while Bragg–Brentano geometry was utilized for operando measurements with a lab-designed operando cell [45]. Operando XRD patterns were captured at 30-minute intervals during cell cycling at 0.2 C.

***Operando* X-ray Absorption Spectroscopy (XAS).** Operando XAS was conducted on NMC samples at various states of charge (SOCs) during the first 1.5 cycles. The *operando* cell was prepared in an argon-filled glove box and then attached to the KMC-2 XANES end station. The NMC and graphite electrodes, each with a diameter of 12 mm, were provided by HAIDI Power company (from the same production batch with the 18650 batteries used for aging tests and post-mortem analyses). The experiment utilized an electrolyte composed of 1 mol of $LiPF_6$ dissolved in 1 liter of solvent, with a composition ratio of EC, DEC, and DMC at 1:1:1. The measurements took place at the XANES end station of the KMC-2 beamline of the BESSY-II synchrotron light source in Berlin, Germany. Pure Ni metal foil samples were simultaneously measured with each NMC sample for accurate energy calibration. Both charging and discharge currents were set at 0.5 C. The DODs were set at 100 %. 75 %, and 45 %. The acquired spectra underwent data processing using the Athena Software package, which included background correction, normalization, k^2-weighting, and Fourier transformation [44,46].

4.4. Correlation analysis

To analyze the correlation between variations of the EIS features, i.e., R_{sei} and R_{ct}, and capacity degradations, correlation coefficients are conducted. Pearson correlation coefficient is good for demonstrating the linear correlation between the features and targets, which helps tell the correlation between the impedance and capacity variations. The expression is denoted as follows [47],

$$\rho(a,b) = \frac{E(ab)}{\sigma_a \sigma_b} \quad \text{(Eq. (1))}$$

Where, $E_{(ab)}$ is the cross-correlation between a and b, and $\sigma_a^2 = E(a^2)$, and $\sigma_b^2 = E(b^2)$ are the variances of the signals a and b, respectively. Here, a represents the impedance (e.g., R_{sei} or R_{ct}), b is the battery SOH.

Associated content

The Supporting Information is available free of charge xxxx.

CRediT authorship contribution statement

Jia Guo: Writing – original draft, Data curation, Writing – review & editing, Investigation, Project administration. **Yaolin Xu:** Validation, Writing – review & editing, Resources, Supervision, Funding acquisition. **Yanchen Liu:** Validation, Data curation. **Pengwei Li:** Validation, Data curation, Formal analysis. **Yunhong Che:** Validation, Visualization, Methodology, Software. **Yaqi Li:** Methodology, Writing – review & editing, Data curation. **Kjeld Pedersen:** Resources, Writing – review & editing, Conceptualization. **Götz Schuck:** Formal analysis, Data curation. **Peter Kjær Kristensen:** Data curation, Formal analysis. **Volodymyr Baran:** Methodology, Data curation, Formal analysis, Investigation. **Yanan Sun:** Methodology, Data curation, Formal analysis. **Philipp Adelhelm:** Funding acquisition, Supervision, Data curation, Writing – review & editing, Formal analysis. **Daniel-Ioan Stroe:** Resources, Funding acquisition, Supervision, Investigation, Writing – review & editing, Methodology.

Declaration of competing interest

We confirm that the manuscript has not been published elsewhere and is not under consideration by any other journal. All authors have approved the submission, and we have no conflicts of interest to declare.

Acknowledgements

The XAS measurements were carried out at the KMC-2 beamline of the BESSY II electron storage ring operated by the Helmholtz-Zentrum Berlin fur Materialien und Energie. The authors thank the beamtime (proposal 231-11967-EF) granted at BESSY II and the help from colleagues Dr. Katherine A. Mazzio, Dr. Yongchun Li and Dr. Dongjiu Xie who helped with the *operando* XAS proposal and measurements. The authors acknowledge the beamtime (proposal I-20221303) granted at DESY (Hamburg, Germany), a member of the Helmholtz Association HGF. Parts of this research were carried out at PETRA III beamline P02.1 and the authors would like to thank colleagues Hui Wang, and Dr. Katherine A. Mazzio who helped with the *ex*-situ XRD measurements. Hui Wang and Dr. Katherine A. Mazzio acknowledge DESY for the support with travel costs. We would like to thank Haidi Company for providing the fresh positive and negative electrodes for *operando*

experiments.

Supplementary materials

Supplementary material associated with this article can be found, in the online version, at doi:10.1016/j.ensm.2025.104441.

References

[1] J.S. Edge, S. O'Kane, R. Prosser, N.D. Kirkaldy, A.N. Patel, A. Hales, A. Ghosh, W. Ai, J. Chen, J. Yang, S. Li, M.C. Pang, L. Bravo Diaz, A. Tomaszewska, M. W. Marzook, K.N. Radhakrishnan, H. Wang, Y. Patel, B. Wu, G.J. Offer, Lithium ion battery degradation: what you need to know, Phys. Chem. Chem. Phys. 23 (2021) 8200–8221, https://doi.org/10.1039/d1cp00359c.

[2] X. Zeng, M. Li, D.Abd El-Hady, W. Alshitari, A.S. Al-Bogami, J. Lu, K. Amine, Commercialization of lithium battery technologies for electric vehicles, Adv. Energy Mater. 9 (2019) 1–25, https://doi.org/10.1002/aenm.201900161.

[3] C. Han, Y. Gao, X. Chen, X. Liu, N. Yao, L. Yu, L. Kong, Q. Zhang, A self-adaptive, data-driven method to predict the cycling life of lithium-ion batteries, InfoMat (2024) 1–9, https://doi.org/10.1002/inf2.12521.

[4] D.M. Davies, M.G. Verde, O. Mnyshenko, Y.R. Chen, R. Rajeev, Y.S. Meng, G. Elliott, Combined economic and technological evaluation of battery energy storage for grid applications, Nat. Energy 4 (2019) 42–50, https://doi.org/10.1038/s41560-018-0290-1.

[5] G. Fukunishi, M. Tabuchi, A. Ikezawa, T. Okajima, F. Kitamura, K. Suzuki, M. Hirayama, R. Kanno, H. Arai, AC impedance analysis of NCM523 composite electrodes in all-solid-state three electrode cells and their degradation behavior, J. Power Sources 564 (2023) 232864, https://doi.org/10.1016/j.jpowsour.2023.232864.

[6] R. Zhang, C. Wang, P. Zou, R. Lin, L. Ma, T. Li, I. hui Hwang, W. Xu, C. Sun, S. Trask, H.L. Xin, Long-life lithium-ion batteries realized by low-Ni, Co-free cathode chemistry, Nat. Energy 8 (2023) 695–702, https://doi.org/10.1038/s41560-023-01267-y.

[7] C.P. Aiken, E.R. Logan, A. Eldesoky, H. Hebecker, J.M. Oxner, J.E. Harlow, M. Metzger, J.R. Dahn, Li[Ni 0.5 Mn 0.3 Co 0.2]O 2 as a superior alternative to LiFePO 4 for long-lived low voltage Li-ion cells, J. Electrochem. Soc. 169 (2022) 050512, https://doi.org/10.1149/1945-7111/ac67b5.

[8] R. Xiong, Y. Pan, W. Shen, H. Li, F. Sun, Lithium-ion battery aging mechanisms and diagnosis method for automotive applications: Recent advances and perspectives, Renew. Sustain. Energy Rev. 131 (2020) 110048, https://doi.org/10.1016/j.rser.2020.110048.

[9] Y. Wu, X. Liu, L. Wang, X. Feng, D. Ren, Y. Li, X. Rui, Y. Wang, X. Han, G.L. Xu, H. Wang, L. Lu, X. He, K. Amine, M. Ouyang, Development of cathode-electrolyte-interphase for safer lithium batteries, Energy Storage Mater. 37 (2021) 77–86, https://doi.org/10.1016/j.ensm.2021.02.001.

[10] A. Geslin, L. Xu, D. Ganapathi, K. Moy, W.C. Chueh, S. Onori, Dynamic cycling enhances battery lifetime, Nat. Energy (2024), https://doi.org/10.1038/s41560-024-01675-8.

[11] C.Y. Wang, T. Liu, X.G. Yang, S. Ge, N.V. Stanley, E.S. Rountree, Y. Leng, B. D. McCarthy, Fast charging of energy-dense lithium-ion batteries, Nature 611 (2022) 485–490, https://doi.org/10.1038/s41586-022-05281-0.

[12] J. Guo, S. Jin, X. Sui, X. Huang, Y. Xu, Y. Li, P.K. Kristensen, D. Wang, K. Pedersen, L. Gurevich, D.I. Stroe, Unravelling and quantifying the aging processes of commercial Li(Ni0.5Co0.2Mn0.3)O2/graphite lithium-ion batteries under constant current cycling, J. Mater. Chem. Mater. 11 (2022) 41–52, https://doi.org/10.1039/d2ta05960f.

[13] W. Guo, Z. Sun, J. Guo, Y. Li, S.B. Vilsen, D.I. Stroe, Digital twin-assisted degradation diagnosis and quantification of NMC battery aging effects during fast charging, Adv. Energy Mater. (2024), https://doi.org/10.1002/aenm.202401644.

[14] S. Müller, P. Pietsch, B.E. Brandt, P. Baade, V. De Andrade, F. De Carlo, V. Wood, Quantification and modeling of mechanical degradation in lithium-ion batteries based on nanoscale imaging, Nat. Commun. 9 (2018), https://doi.org/10.1038/s41467-018-04477-1.

[15] S. Micari, S. Foti, A. Testa, S. De Caro, F. Sergi, L. Andaloro, D. Aloisio, S. G. Leonardi, G. Napoli, Effect of WLTP CLASS 3B driving cycle on lithium-ion battery for electric vehicles, Energies 15 (2022) 1–25, https://doi.org/10.3390/en15186703.

[16] J. Guo, Y. Li, K. Pedersen, D.I. Stroe, Lithium-ion battery operation, degradation, and aging mechanism in electric vehicles: an overview, Energies 14 (2021) 1–22, https://doi.org/10.3390/en14175220.

[17] R. Gauthier, A. Luscombe, T. Bond, M. Bauer, M. Johnson, J. Harlow, A. Louli, J. R. Dahn, How do depth of discharge, C-rate and calendar age affect capacity retention, impedance growth, the electrodes, and the electrolyte in Li-ion cells? J. Electrochem. Soc. 169 (2022) 020518 https://doi.org/10.1149/1945-7111/ac4b82.

[18] L.K. Willenberg, P. Dechent, G. Fuchs, D.U. Sauer, E. Figgemeier, High-Precision monitoring of volume change of commercial lithium-ion batteries by using strain gauges, Sustainability 12 (2020) 557, https://doi.org/10.3390/su12020557.

[19] A. Eldesoky, N. Kowalski, J.R. Dahn, Highlighting the advantages of operating NMC811 cells to voltages below 4.20 V compared to NMC grades with lower Ni content, J. Electrochem. Soc. 170 (2023) 080515, https://doi.org/10.1149/1945-7111/aceffd.

[20] M.T. Lawder, P.W.C. Northrop, V.R. Subramanian, Model-based SEI layer growth and capacity fade analysis for EV and PHEV batteries and drive cycles, J. Electrochem. Soc. 161 (2014) A2099–A2108, https://doi.org/10.1149/2.1161412jes.

[21] L. Wildfeuer, A. Karger, D. Aygül, N. Wassiliadis, A. Jossen, M. Lienkamp, Experimental degradation study of a commercial lithium-ion battery, J. Power Sources 560 (2023) 232498, https://doi.org/10.1016/j.jpowsour.2022.232498.

[22] Y. Gao, J. Jiang, C. Zhang, W. Zhang, Y. Jiang, Aging mechanisms under different state-of-charge ranges and the multi-indicators system of state-of-health for lithium-ion battery with Li(NiMnCo)O2 cathode, J. Power Sources 400 (2018) 641–651, https://doi.org/10.1016/j.jpowsour.2018.07.018.

[23] M. Lewerenz, P. Dechent, D.U. Sauer, Investigation of capacity recovery during rest period at different states-of-charge after cycle life test for prismatic Li(Ni 1/3 Mn 1/3 Co 1/3)O 2 -graphite cells, J. Energy Storage 21 (2019) 680–690, https://doi.org/10.1016/j.est.2019.01.004.

[24] L. Wildfeuer, A. Karger, D. Aygül, N. Wassiliadis, A. Jossen, M. Lienkamp, Experimental degradation study of a commercial lithium-ion battery, J. Power Sources 560 (2023) 232498, https://doi.org/10.1016/j.jpowsour.2022.232498.

[25] S.J. Park, Y.W. Song, B.S. Kang, W.J. Kim, Y.J. Choi, C. Kim, Y.S. Hong, Depth of discharge characteristics and control strategy to optimize electric vehicle battery life, J. Energy Storage 59 (2023) 106477, https://doi.org/10.1016/j.est.2022.106477.

[26] I.J. Fernández, C.F. Calvillo, A. Sánchez-Miralles, J. Boal, Capacity fade and aging models for electric batteries and optimal charging strategy for electric vehicles, Energy 60 (2013) 35–43, https://doi.org/10.1016/j.energy.2013.07.068.

[27] C. Pastor-Fernández, K. Uddin, G.H. Chouchelamane, W.D. Widanage, J. Marco, A comparison between electrochemical impedance spectroscopy and incremental capacity-differential voltage as Li-ion diagnostic techniques to identify and quantify the effects of degradation modes within battery management systems, J. Power Sources 360 (2017) 301–318, https://doi.org/10.1016/j.jpowsour.2017.03.042.

[28] S.K. Jung, H. Gwon, J. Hong, K.Y. Park, D.H. Seo, H. Kim, J. Hyun, W. Yang, K. Kang, Understanding the degradation mechanisms of LiNi0.5Co 0.2Mn0.3O2 cathode material in lithium ion batteries, Adv. Energy Mater. 4 (2014) 1–7, https://doi.org/10.1002/aenm.201300787.

[29] J. Guo, Y. Li, J. Meng, K. Pedersen, L. Gurevich, D.I. Stroe, Understanding the mechanism of capacity increase during early cycling of commercial NMC/graphite lithium-ion batteries, J. Energy Chem. 74 (2022) 34–44, https://doi.org/10.1016/j.jechem.2022.07.005.

[30] J. Guo, Y. Che, K. Pedersen, D.I. Stroe, Battery impedance spectrum prediction from partial charging voltage curve by machine learning, J. Energy Chem. 79 (2023) 211–221, https://doi.org/10.1016/j.jechem.2023.01.004.

[31] S. Liu, L. Wang, C. Zhang, B. Chu, C. Wang, T. Huang, A. Yu, Dynamic evolution of cathode−electrolyte interface of LiNi0.6Co0.2Mn0.2O2 during the initial charge−discharge process, J. Power Sources 438 (2019) 226979, https://doi.org/10.1016/j.jpowsour.2019.226979.

[32] X. Zheng, Z. Cao, W. Luo, S. Weng, X. Zhang, D. Wang, Z. Zhu, H. Du, X. Wang, L. Qie, H. Zheng, Y. Huang, Solvation and interfacial engineering enable −40 °C operation of graphite/NCM batteries at energy density over 270 Wh kg $^{-1}$, Adv. Mater. 35 (2023), https://doi.org/10.1002/adma.202210115.

[33] Y. Li, J. Guo, K. Pedersen, L. Gurevich, D.I. Stroe, Investigation of multi-step fast charging protocol and aging mechanism for commercial NMC/graphite lithium-ion batteries, J. Energy Chem. 80 (2023) 237–246, https://doi.org/10.1016/j.jechem.2023.01.016.

[34] R. Li, W. Li, A. Singh, D. Ren, Z. Hou, M. Ouyang, Effect of external pressure and internal stress on battery performance and lifespan, Energy Storage Mater. 52 (2022) 395–429, https://doi.org/10.1016/j.ensm.2022.07.034.

[35] J. Guo, Y. Li, J. Meng, K. Pedersen, L. Gurevich, D.I. Stroe, Understanding the mechanism of capacity increase during early cycling of commercial NMC/graphite lithium-ion batteries, J. Energy Chem. 74 (2022) 34–44, https://doi.org/10.1016/j.jechem.2022.07.005.

[36] G.A. Elia, G. Greco, P.H. Kamm, F. García-Moreno, S. Raoux, R. Hahn, Simultaneous X-ray diffraction and tomography operando investigation of aluminum/graphite batteries, Adv. Funct. Mater. 30 (2020) 1–9, https://doi.org/10.1002/adfm.202003913.

[37] J. Guo, Y. Xu, M. Exner, X. Huang, Y. Li, Y. Liu, H. Wang, J. Kowal, Q. Zhang, P. K. Kristensen, D. Wang, K. Pedersen, L. Gurevich, D. Stroe, P. Adelhelm, Unravelling the mechanism of pulse current charging for enhancing the stability of commercial LiNi 0.5 Mn 0.3 Co 0.2 O 2 /graphite lithium-ion batteries, Adv. Energy Mater. 2400190 (2024) 1–14, https://doi.org/10.1002/aenm.202400190.

[38] J. Guo, S. Jin, X. Sui, X. Huang, Y. Xu, Y. Li, P.K. Kristensen, D. Wang, K. Pedersen, L. Gurevich, D.-I. Stroe, Unravelling and quantifying the aging processes of commercial Li(Ni 0.5 Co 0.2 Mn 0.3)O 2 /graphite lithium-ion batteries under constant current cycling, J. Mater. Chem. Mater. 11 (2023) 41–52, https://doi.org/10.1039/D2TA05960F.

[39] Z. Tan, X. Chen, Y. Li, X. Xi, S. Hao, X. Li, X. Shen, Z. He, W. Zhao, Y. Yang, Enabling superior cycling stability of $LiNi_{0.9}Co_{0.05}Mn_{0.05}O_2$ with controllable internal strain, Adv. Funct. Mater. 33 (2023), https://doi.org/10.1002/adfm.202215123.

[40] Y.H.T. Tran, K. An, D.T.T. Vu, S.-W. Song, High-voltage electrolyte and interface design for mid-nickel high-energy Li-ion batteries, ACS Energy Lett. (2024) 356–370, https://doi.org/10.1021/acsenergylett.4c02860.

[41] J. Zhao, X. Feng, M.-K. Tran, M. Fowler, M. Ouyang, A.F. Burke, Battery safety: fault diagnosis from laboratory to real world, J. Power Sources 598 (2024) 234111, https://doi.org/10.1016/j.jpowsour.2024.234111.

[42] A.C. Dippel, H.P. Liermann, J.T. Delitz, P. Walter, H. Schulte-Schrepping, O. H. Seeck, H. Franz, Beamline P02.1 at PETRA III for high-resolution and high-energy powder diffraction, J. Synchrotron. Radiat. 22 (2015) 675–687, https://doi.org/10.1107/S1600577515002222.

[43] J. Filik, A.W. Ashton, P.C.Y. Chang, P.A. Chater, S.J. Day, M. Drakopoulos, M. W. Gerring, M.L. Hart, O.V. Magdysyuk, S. Michalik, A. Smith, C.C. Tang, N. J. Terrill, M.T. Wharmby, H. Wilhelm, Processing two-dimensional X-ray diffraction and small-angle scattering data in DAWN 2, J. Appl. Crystallogr. 50 (2017) 959–966, https://doi.org/10.1107/S1600576717004708.

[44] B. Ravel, M. Newville, ATHENA, ARTEMIS, HEPHAESTUS: data analysis for X-ray absorption spectroscopy using IFEFFIT, J Synchrotron Radiat. (2005) 537–541, https://doi.org/10.1107/S0909049505012719.

[45] W. Xu, Y. Xu, V. Grzimek, A. Martin, T. Schultz, P.A. Russo, Y. Lu, N. Koch, N. Pinna, Insights into the kinetics–morphology relationship of 1-, 2-, and 3D TiNb2O7 anodes for Li-ion storage, Nano Res. 6 (2023) 1–11, https://doi.org/10.1007/s12274-023-6201-1.

[46] S.D. Kelly, K.M. Kemner, J.B. Fein, D.A. Fowle, M.I. Boyanov, B.A. Bunker, N. Yee, X-ray absorption fine structure determination of pH-dependent U-bacterial cell wall interactions, Geochim. Cosmochim. Acta 66 (2002) 3855–3871, https://doi.org/10.1016/S0016-7037(02)00947-X.

[47] J. Benesty, J. Chen, Y. Huang, I. Cohen, Pearson correlation coefficient. Springer Topics in Signal Processing, Springer Science and Business Media B.V, 2009, pp. 1–4, https://doi.org/10.1007/978-3-642-00296-0_5.